

# Anatomical-Functional Image Fusion by Information of Interest in Local Laplacian Filtering Domain

Jiao Du, Weisheng Li, and Bin Xiao

**Abstract**—A novel method for performing anatomical magnetic resonance imaging-functional (positron emission tomography or single photon emission computed tomography) image fusion is presented. The method merges specific feature information from input image signals of a single or multiple medical imaging modalities into a single fused image, while preserving more information and generating less distortion. The proposed method uses a local Laplacian filtering-based technique realized through a novel multi-scale system architecture. First, the input images are generated in a multi-scale image representation and are processed using local Laplacian filtering. Second, at each scale, the decomposed images are combined to produce fused approximate images using a local energy maximum scheme and produce the fused residual images using an information of interest-based scheme. Finally, a fused image is obtained using a reconstruction process that is analogous to that of conventional Laplacian pyramid transform. Experimental results computed using individual multi-scale analysis-based decomposition schemes or fusion rules clearly demonstrate the superiority of the proposed method through subjective observation as well as objective metrics. Furthermore, the proposed method can obtain better performance, compared with the state-of-the-art fusion methods.

**Index Terms**—Image fusion, multi-scale decomposition, interest-based rule.

## I. INTRODUCTION

MULTIPLE medical imaging data allows for increased performance in a wide range of clinical applicability of medical images for diagnosis and assessment of medical problems [1]. Over the past decades, anatomical-functional fusion systems such as MRI-PET and MRI-SPECT have been seen as a new hybrid molecular imaging technology [2], [3]. MRI image provides anatomical contrast of soft-tissue structure at a high spatial resolution. However, it lacks activity

Manuscript received November 21, 2016; revised May 16, 2017 and July 20, 2017; accepted August 17, 2017. Date of publication August 25, 2017; date of current version September 21, 2017. This work was supported in part by the Natural Science Foundation of China under Grant 61272195, Grant 61472055, and Grant U1401252, in part by the Chongqing Outstanding Youth Fund under Grant cstc2014jcyjjq40001, and in part by the Chongqing Research Program of Application Foundation and Advanced Technology under Grant cstc2012jJA1699. The associate editor coordinating the review of this manuscript and approving it for publication was Prof. Jan Sijbers. (*Corresponding author: Weisheng Li*)

J. Du is with the Chongqing Engineering Laboratory for Detection, Control and Integrated System, Chongqing Technology and Business University, Chongqing 400067, China (e-mail: dujiao19880429@126.com).

W. Li and B. Xiao are with the Chongqing Key Laboratory of Computational Intelligence, Chongqing University of Posts and Telecommunications, Chongqing 400065, China (e-mail: liws@cqupt.edu.cn; xiaobin@cqupt.edu.cn).

Color versions of one or more of the figures in this paper are available online at <http://ieeexplore.ieee.org>.

Digital Object Identifier 10.1109/TIP.2017.2745202

information about soft tissues. In contrast, PET images provide high contrast for accurately tracing tumors. SPECT imaging is used to study blood flow in tissues and organs using nuclear imaging techniques. However, PET and SPECT images have low resolution. The goal of an MRI-PET or MRI-SPECT system is to merge multiple images from a single or from multiple imaging modalities into a fused image while preserving specific feature information. The benefits of an MRI-PET or MRI-SPECT system can be achieved by simple image fusion for some basic clinical brain examinations because the skull provides a frame of reference for the soft tissue of the brain [4]–[6]. In this paper, we focus on image fusion methods for MRI-PET or MRI-SPECT systems in the clinical study of brain tumors.

The available multi-modal medical image fusion methods can be performed at the pixel level, feature level, and decision level depending on the format in which the image information is processed [7]. Medical image fusion methods at the pixel level combine information in a raw image pixel representation. Fusion methods at the feature level are performed on a feature-by-feature basis, such as by processing edge information and detail information. Fusion methods at the decision level refer to making a final decision based on the fused image. Due to the advantages of low computational complexity and simple implementation, a large number of research papers have focused on pixel-level fusion methods. Therefore, an image fusion method at the pixel level is presented in this paper.

Multi-modal pixel-level medical image fusion has attracted a considerable amount of attention in recent years. Multi-scale analysis (MSA) tools have achieved the best fusion performance [8], [9]. In contrast to single-scale based fusion methods, MSA-based fusion methods have the advantage of extracting and combining much more image feature information at different scales. MSA-based fusion methods can be summarized by the following steps: image decomposition, image fusion rule construction and adoption, and image reconstruction. Image decomposition is performed first by transforming the input images into their multi-scale image representations. The process separates the image signals into sub-band images at high-frequency and low-frequency resolutions. The high-frequency images contain more detailed information from the original images, while the low-frequency images provide coarser image features. The fusion scheme then creates new image fusion rules for combining the high-frequency images and low-frequency images. After obtaining

the fused high-frequency images and the fused low-frequency images, the inverse image decomposition transform is used to reconstruct the output fused image.

Traditionally, image decomposition in MSA can be divided into two categories: the pyramid transform [10]–[16] and the parallelepiped transform [17]–[19]. In the first class of fusion methods such as the Laplacian pyramid transform (LAP) [10], gradient pyramid transform (GRP) [11], curvelet transform (CVT) [12], contourlet transform (COT) [13] and shearlet transform (ST) [14], each level of the sub-band image results from subsampling the corresponding level. The subsampled sub-band at each level is the result of the successive reduction by a factor of 2 of the image resolution in the pyramid transform domain. However, these kinds of methods may produce some distortion in the resulting image, which appears obvious when considering the subsampling algorithm. The second class of fusion methods was proposed to fuse multiple images using a nonsubsampling process in a multi-scale scheme. In the parallelepiped scheme, all approximated images have the same number of columns and rows as the input images using the image filter filled with zeroes. When climbing up through the resolution levels, the successive approximation images have a coarser resolution while remaining the same size as the input images. Parallelepiped-based fusion methods, such as the nonsubsampled contourlet transform (NSCT) [17], the support value transform (SVT) [18], and the neighborhood distance transform (ND) [19], have been recognized as efficient shift-invariant image representations. NSCT [15] was developed from the nonsubsampled LAP and the nonsubsampled directional filter bank. In addition, SVT [18] is constructed by combining nonsubsampled LAP and a support value filter. In addition, ND [19] is constructed by combining nonsubsampled LAP and a neighborhood distance filter. However, a drawback of these methods is the higher computational time of parameter initialization.

In addition to image decomposition, the other key step is to adopt efficient image fusion rules for combining approximate low-frequency images and residual high-frequency images. The approximate low-frequency images provide similar information from the input images. Moreover, the residual high-frequency images present salient feature information from the different inputs. The generic average-maximum fusion scheme denotes that the fused low-frequency image is the average of the corresponding coefficients of the input images, and the fused high-frequency image is calculated using the maximum scheme. However, the average-maximum fusion scheme always generates unsatisfactory results such as artifacts. Later, much more effective schemes such as principal component analysis (PCA) [20], general intensity-hue-saturation (GIHS) [21], pulse coupled neural network (PCNN) [22], [23], sparse representation (SR) [24], dense scale invariant feature transform (DSIFT) [8], and Smallest Univalue Segment Assimilating Nucleus (SUSAN) [25] were developed to fuse the decomposed coefficients. GIHS methods can retain more of the spatial resolution of the input anatomical medical image by way of substituting high resolution for intensity. PCA, PCNN and SR methods are all based on the assumption

that input images with different modalities can express salient feature information. In PCA [20], the fused image is a combination of the principal components of the inputs. In particular, PCNN and SR methods usually include two stages: training and testing [22]–[24]. In the first stage, a large number of images are used in training to achieve optimal image pixel values. In the second stage, the fused image is obtained by implementing arithmetic operators on the trained optimal image pixel values. However, PCNN and SR methods take a long time because of the training stage. To incorporate spatial information, the DSIFT and SUSAN descriptors are adopted to detect points of interest, with the purpose of preserving prominent texture and edge information in the input image [8], [24].

Two directions can be explored with the existing MSA methods for medical image fusion to improve the quality of the fused image: advanced image decomposition schemes and effective image fusion rules. In this paper, we propose a method for fusing an anatomical image and a functional image through advanced image decomposition and effective image fusion rules. In the proposed method, local Laplacian filtering (LLF) [26] is selected as the multi-scale image decomposition tool for processing the input MRI, PET, and SPECT images. It can be clearly observed that LAP is the basis of MSA tools, as mentioned above. However, traditional LAP is unable to represent edge information well. To overcome this limitation, LLF [26] is used not only to preserve structural information but also to enhance detail information. Then, two image fusion rules are constructed for combining the approximate and residual images. For the approximate images, the energy of each center pixel of the local region is first defined as the sum of itself and nearby pixel values. Then, by selecting one pixel with the maximum local energy using the local energy maximum (LEM) method, gradient information is preserved in the fused approximate image. Inspired by the DSIFT and SUSAN methods [8], [24], an information of interest (IOI)-based fusion rule is adopted to combine the residual images [27]. What is IOI in the content of an image? The anatomical image provides structural information about the tissue type of the human brain, while the functional image presents high-intensity levels where activity occurs. Thus, structural information and high intensity define IOI in the anatomical and functional images. To make full use of IOI, the local extrema scheme (LES) [28] is used to enhance the detail information of the input anatomical image, and gradient orientation information based on spatial frequencies (SF) [29] is used to outline the abnormal region of the input functional image. Finally, the fused image is obtained using the revised traditional pyramid transform. The superiority of the proposed method is demonstrated via experimental results obtained using both subjective and objective evaluation tools.

The rest of this paper is organized as follows. In Section II, the local Laplacian filtering is reviewed. Section III describes the proposed fusion method in terms of the advanced image decomposition scheme and the effective image fusion rules. The experiments on groups of MRI-PET and MRI-SPECT image fusion are presented in Section IV. Finally, Section V gives the conclusion.

TABLE I  
IMPORTANT NOTATION AND TERMS USED IN THIS PAPER

$A, B, F$	Anatomical, functional, fused images, for respectively.
$R_A^i, R_{A+}^i, R_{A-}^i$	Residual image of anatomical medical image at the $i$ -th scale, IOI and UIOI in residual image at the $i$ -th scale, for respectively.
$R_B^i, R_{B+}^i, R_{B-}^i$	Residual image of functional medical image at the $i$ -th scale, IOI and UIOI in functional image at the $i$ -th scale, for respectively.
$R_F^i, R_{F+}^i, R_{F-}^i$	Fused residual image at the $i$ -th scale, fused IOI and fused UIOI in residual image at the $i$ -th scale, for respectively.
$G_A^i, G_B^i, G_F^i$	Approximate image of anatomical and functional medical images, fused approximate image at the $i$ -th scale, for respectively.
$\times, \sim$	Component-wise multiplication and logic operation of not with the values of 0 and 1.

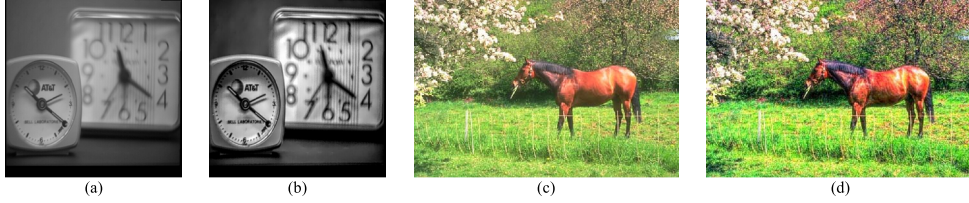


Fig. 1. The filtered images acquired by applying LLF to grayscale and RGB images. (a) Input gray image. (b) Gray image after LLF. (c) Input RGB image. (d) RGB image after LLF.

## II. LOCAL LAPLAICAN FILTERING

Edge-preserving filters enhance detail information in an image while preserving the sharpness of its edge information. Edge-preserving filters have wide applications in the fields of medical imaging, such as medical image restoration [30], medical image denoising [31], and medical image fusion [32]–[35]. In the field of medical image fusion, authors have constructed new multi-scale image decomposition and reconstruction schemes [33]–[35] and new image fusion rules based on edge-preserving filters [32]. The advantage of edge-preserving filters in medical image fusion is that medical images can be fused and enhanced simultaneously. In the proposed method, LLF [26], an edge-preserving filter, is adopted as the multi-scale image decomposition and reconstruction tool. Compared with other edge-preserving filters, the advantages of LLF [26] are that: (1) LLF is based on the traditional standard Laplacian pyramid method. (2) LLF operates on raw pixels rather than solving an optimization problem. (3) LLF models edge information in an input image using a simple threshold of pixel values to differentiate large-scale edge information from small-scale detail information. LAP filtering has been applied to fuse medical images with different modalities at multiple scales. However, the fused image introduces degrading edges and halos. To overcome these limitations, LLF [26] is proposed, given its advantages of simplicity and flexibility. Please refer to Table I for important definitions used throughout the rest of this paper.

In theory, LLF assumes that the filtered output  $O$  is constructed by computing a new LAP for the intermediate image coefficients  $S[I']$  at each scale  $i$ .

$$O = \text{collapse}(S_i[I']). \quad (1)$$

For each coefficient  $v = (x, y, i)$  in the image  $I'$ , we generate a new coefficient  $I'(v)$  by applying a point-wise remapping

function,

$$I'(v) = \begin{cases} g + \text{sign}(v - g)\sigma_r(|v - g|/\sigma_r)^\alpha, & \text{if } |v - g| \leq \sigma_r \\ g + \text{sign}(v - g)(\beta(|v - g| - \sigma_r) + \sigma_r), & \text{otherwise,} \end{cases} \quad (2)$$

where  $(x, y)$  represents the pixel coordinate in horizontal orientation and vertical orientation,  $i$  represents the level of the pyramid, sign denotes signal function,  $v$  is the pixel value at the position  $(x, y)$ , and  $g$  is value of the image resulting from the Gaussian pyramid.

Furthermore, in (2) there are three free parameters in LLF: the intensity threshold  $\sigma_r$ , the detail parameter  $\alpha$ , and the edge parameter  $\beta$ . (1) The intensity threshold  $\sigma_r$  acts as the threshold for differentiating edge information from detail information. If  $|v - g| \leq \sigma_r$ ,  $v$  should be processed as detail information. Otherwise,  $v$  should be processed as edge information. (2) The detail parameter  $\alpha$  is closely related to detail information. (3) The edge parameter  $\beta$  is closely related to edge information. If  $0 < \alpha < 1$  and  $\beta = 1$ , LLF of the input image is a detail enhancement operation. If  $\alpha = 1$  and  $0 \leq \beta < 1$ , LLF of the input image is edge-aware compression. If  $\alpha = 1$  and  $\beta = 1$ , the input image coefficient is not changed. Moreover, for a color input image, the filtered output is obtained by applying LLF to the red, green, and blue (RGB) channels of the input image. In conclusion, when the edge parameter  $\beta = 1$ , LLF evolves into filtering of details [26]. In the proposed method, we want to preserve the edge sharpness and enhance detail information in the fused image. Therefore, the edge parameter  $\beta$  is set at 1. In addition, after many experiments, the intensity threshold  $\sigma_r$  was set at 0.4 and the detail parameter  $\alpha$  was set at 0.25. Examples of filtered images after LLF are shown in Fig. 1. It can be observed that LLF enhances detail information in

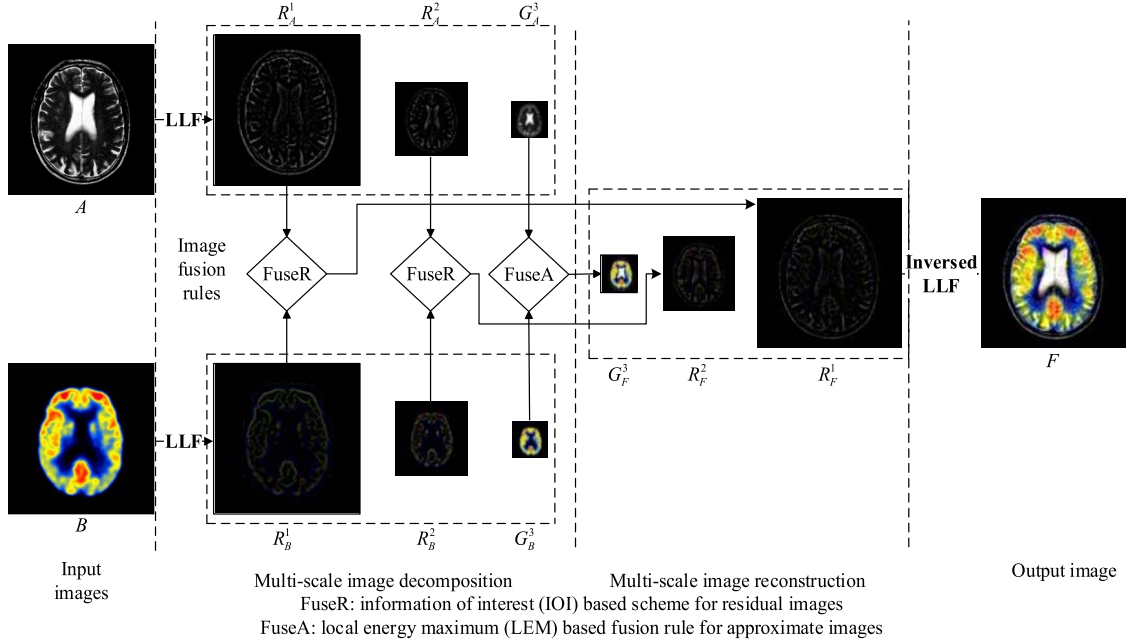


Fig. 2. Schematic diagram of local Laplacian filtering with the length of 3 based fusion method.

#### Algorithm 1 Basic Steps of the Anatomical-Functional Image Fusion (MRI-PET or MRI-SPECT)

Input: anatomical image (MRI)  $A$ , functional image (PET or SPECT)  $B$

Output: the fused image  $F$

Step 1: multi-scale image decomposition

Apply  $L$ -level LLF method to decompose  $A$  and  $B$  into approximate and residual images at various levels  $(R_i^1, G_A^1), (R_i^2, G_A^2), \dots, (R_i^L, G_A^L)$  and  $(R_B^1, G_B^1), (R_B^2, G_B^2), \dots, (R_B^L, G_B^L)$  with  $i = 1 \sim L-1$  ( (3) ).

Step 2: image fusion rules

(1) Estimate the fused approximate image  $G_F^L$  using the LEM-based fusion rule on approximate image  $G_A^L, G_B^L$  of  $A$  and  $B$  ( (4)-(8) ).

(2) Apply the LES+SOI method to decompose  $A$  into IOI  $R_{A+}^i$  and UIOI  $R_{A-}^i$ , and apply SF+SOI method to decompose  $B$  into IOI  $R_{B+}^i$  and UIOI  $R_{B-}^i$  ( (9) and (10) ).

(3) Apply the LEM-based fusion rule on IOI of  $A$  and  $B$  to get the fused IOI  $R_{F+}^i$  and apply an AVG-based fusion rule on the UIOI of  $A$  and  $B$  to get the fused UIOI  $R_{F-}^i$  ( (4), (11) and (12) ).

(4) Estimate the fused residual image:  $R_F^i = \text{AOI}(R_{F+}^i, R_{F-}^i)$  using AOI function to combine the fused IOI  $R_{F+}^i$  and the fused UIOI  $R_{F-}^i$  ( (13) ).

Step 3: multi-scale image reconstruction

Obtain the fused image:  $\sum_{i=1}^{L-1} R_F^i + G_F^L = F$ .

both the grayscale image and the RGB image in Fig. 1. As shown in Fig. 1(a), the input grayscale image contains one clock in focus and one clock out of focus. After the operation of LLF, the filtered image shows that the two clocks are clear. For the RGB image, the filtered image has higher contrast. In particular, the texture information of the horse in the filtered image is clear. Furthermore, the tree in the filtered image is enhanced by LLF.

### III. PROPOSED METHOD

The main steps of the proposed method for MRI-PET or MRI-SPECT fusion are summarized in Fig. 2 and Algorithm 1. In Algorithm 1, the proposed fusion method includes three steps: multi-scale image decomposition using

LLF, application of image fusion rules using IOI, and multi-scale image reconstruction using the inverse LLF. From Fig. 2, it can be observed that the image fusion rule contains FuseR and FuseA in the proposed fusion method. FuseR denotes that IOI is used as the image fusion rule for residual images decomposed by LLF, and FuseA denotes that LEM is used as the image fusion rule for approximated images decomposed by LLF.

#### A. Input

The input images are anatomical (MRI) and functional (PET or SPECT) medical imaging data. MRI image, defined as a structural medical image, provides information about the tissue type of the human brain at high spatial

---

**Algorithm 2** Basic Steps of Local Energy Maximum
 

---

Input: approximate image of anatomical image  $G_A^L$  and approximate image of functional medical images  $G_B^L$

Output: the fused approximate image  $G_F^L$

Step 1: Calculate the local energy  $E_\mu(x, y)$  of approximate image coefficients  $G_\mu^L (\mu = A, B)$ ,

$$E_\mu(x, y) = \sum_{i=1}^w \sum_{j=1}^w [G_\mu^L(x+i, y+j)]^2 \times W_e(i, j), \quad (4)$$

where  $(x, y)$  denotes the pixel to be processed in the image  $G_A^L, G_B^L$ , where  $w$  denotes the local window size ( $w = 3$ ), and where  $W_e$  is a  $3 \times 3$  filtering template defined as,

$$W_e = [1, 1, 1; 1, 1, 1; 1, 1, 1]. \quad (5)$$

Step 2: Choose the maximum value in the neighborhood by filtering with a  $3 \times 3$  window to determine the local energy  $E_\mu(x, y)$ ,

$$F_\mu(x, y) = \max \{E_\mu(x+i, y+j) | 1 \leq i, j \leq 3\}. \quad (6)$$

Step 3: Calculate the binary decision map  $M(x, y)$

$$M(x, y) = \begin{cases} 1, & \text{if } F_A(x, y) > F_B(x, y) \\ 0, & \text{otherwise} \end{cases}. \quad (7)$$

Step 4: Obtain the fused approximate image coefficients  $G_F^L(x, y)$

$$G_F^L(x, y) = M(x, y) \times G_A^L(x, y) + \sim M(x, y) \times G_B^L(x, y). \quad (8)$$


---

resolution. Meanwhile, PET and SPECT images are defined as functional images, providing information on blood flow and biological activity with low spatial resolution. The input images are assumed to be co-registered, which is a common assumption in multi-modal medical image fusion. Let  $A$  and  $B$  denote the input anatomical and functional image, respectively.

### B. Multi-Scale Image Decomposition

A single image can be decomposed into an approximate image and a series of residual images by LLF. The approximate images  $G$  provides low-frequency information, such as the basic outline of the brain. Unlike the approximate image, the residual images  $R$  provide high-frequency information, such as edge information and texture information. In (3), parameter  $L$  is the step length in the proposed method. Length  $L$  is related to subjective and objective evaluations of the fused image. A discussion of length  $L$  is provided in Section IV.B.

$$A = \sum_{i=1}^{L-1} R_A^i + G_A^L, \quad B = \sum_{i=1}^{L-1} R_B^i + G_B^L. \quad (3)$$

### C. Image Fusion Rules

Image fusion rules refer to algorithms that seek to highlight features of interest in the original image. Traditionally, image fusion rules contain three components: activity-level measurements, coefficient grouping, and coefficient combination [36], [37].

- 1) Activity-level measurements: The activity-level scheme measures the salient features of each coefficient at various scales.
- 2) Coefficient grouping: The coefficient grouping scheme uses a strategy for grouping the corresponding coefficients.

3) Coefficient combination: The coefficient combination aims to combine coefficients at different scales with differently weighted functions.

*1) Local Energy Maximum Based Fusion Rules for Approximate Images:* The approximate images determined by LLF provide an approximation of the input medical images. Generally, the average (AVG) scheme has been used to fuse the approximate images from the anatomical and functional medical images. However, the resulting fused image introduces ringing artifacts. To pass information within and between each decomposition level to achieve inter-scale dependencies, the fused approximate image should be capable of preserving more low-pass information from the input images. LEM was adopted since it has the advantage of preserving much more regional information using the local energy function in Algorithm 2.

*2) Information of Interest Based Fusion Rules for Residual Images:* For the residual images, IOI scheme is selected as the fusion rules. It includes two steps:

(1) To obtain IOIs of the residual images: LES and SF are adopted to distinguish the IOI from the un-interest of information (UIOI) [28], [29]. For the anatomical image, LES is used to obtain the UIOI with  $R_{A-}^i = \text{LES}(R_A^i, k)$  in which the default value of the parameter is  $k = 3$ . Usually, the rest of the image is easily obtained by subtracting the UIOI from the input residual images. However, image subtraction using the arithmetic minus operator introduces color distortion because there are many pixel values in the image that are negative. In this study, the subtraction-of-image (SOI) function is defined to obtain the IOI of the residual anatomical image,

$$R_{A+}^i(x, y) = \begin{cases} R_A^i(x, y) - R_{A-}^i(x, y), & \text{if } R_A^i(x, y) > R_{A-}^i(x, y) \\ R_A^i(x, y), & \text{otherwise.} \end{cases} \quad (9)$$

For the functional image, SF is adopted as the decomposition scheme for detecting the IOI from the residual functional images ( $R_{B+}^i = SF(R_B^i)$ ). In addition, the UIOI of the residual functional image is calculated by the SOI function,

$$R_{B-}^i(x, y) = \begin{cases} R_B^i(x, y) - R_{B+}^i(x, y), & \text{if } R_B^i(x, y) > R_{B+}^i(x, y) \\ R_B^i(x, y), & \text{otherwise.} \end{cases} \quad (10)$$

(2) The fused residual image is obtained as follows. The LEM scheme is chosen for combining decomposed IOIs from the anatomical and functional images. The fused IOI,  $R_{F+}^i$  is defined as,

$$R_{F+}^i = \begin{cases} R_{A+}^i, & \text{if } E_{A+}^i > E_{B+}^i \\ R_{B+}^i, & \text{otherwise,} \end{cases} \quad (11)$$

where  $E$  are the pixel values of the local energy defined in (4) with a window size of  $3 \times 3$ . The AVG scheme is chosen for combining decomposed UIOIs from the anatomical and functional images. The fused UIOI is defined as,

$$R_{F-}^i = 0.5 \times (R_{A-}^i + R_{B-}^i). \quad (12)$$

Then, corresponding to SOI function, an addition-of-image (AOI) function is designed to combine the fused IOI  $R_{F+}^i$  and the fused UIOI  $R_{F-}^i$ ,

$$R_F^i(x, y) = \begin{cases} R_{F+}^i(x, y), & \text{if } R_{F+}^i(x, y) = R_{F-}^i(x, y) \\ R_{F+}^i(x, y) + R_{F-}^i(x, y), & \text{otherwise.} \end{cases} \quad (13)$$

#### D. Multi-Scale Image Reconstruction

The fused image is obtained by multi-scale image reconstruction scheme. Fusion methods in the frequency domain usually apply the inverse transform scheme used in multi-scale image decomposition. According to the multi-scale image decomposition shown in (3), the fused image is obtained using the inverse of equation (2). Thus, after the fusion of the approximate images and the residual images, the fused images at each scale  $i$  are combined according to the inverse LLF, namely,

$$\sum_{i=1}^{L-1} R_F^i + G_F^L = F. \quad (14)$$

## IV. EXPERIMENTS

First, this section illustrates the basic setting of the experiments including the test data and the objective image quality metrics. Then, the experimental results and a discussion about the 60 sets of anatomical and functional medical images provided.

#### A. Experimental Settings

The testing imaging data include anatomical MRI images in high resolution and functional PET and SPECT images in pseudo-color. All the test data are downloaded from the online database established by Harvard Medical School [38]. The resolution of the MRI, PET, and SPECT test data was

$256 \times 256$  pixels, and the images were co-registered. The test data have been used in many image fusion methods [39]–[41]. Compared to PET and SPECT images, MRI image provides higher per pixel contrast of the soft tissue of the brain.

To access the fused images resulting from different methods, ten objective image quality metrics (i.e., structural similarity (*SSIM*) [42], standard (*STD*) [24], edge intensity (*EI*) [43], [44], *SF* [29], average gradient (*AG*) [45], [46], mutual information (*MI*) [47], gradient magnitude similarity (*GMS*) [48], visual information fidelity (*VIF*) [49], tone-mapped image quality index (*TMQI*) [50], and spatial-spectral entropy-based quality index (*SSEQ*) [51]) are adopted. The larger the metrices including *SSIM*, *STD*, *EI*, *SF*, *AG*, *MI*, *GMS*, *VIF*, and *TMQI*, the better the quality of the fused image is. The smaller the metric *SSEQ* is, the better the quality of the fused image is. The following metrics are used to evaluate the performance of the fused results, with and without the reference image. Readers can refer to these references for more detail about how they are computed.

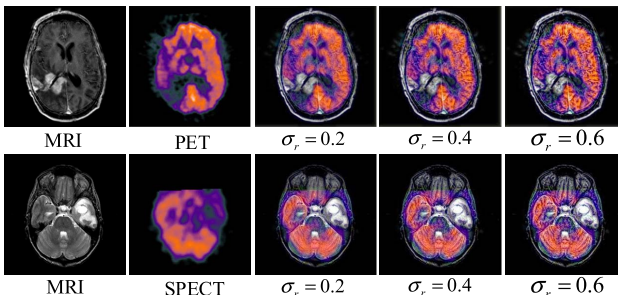
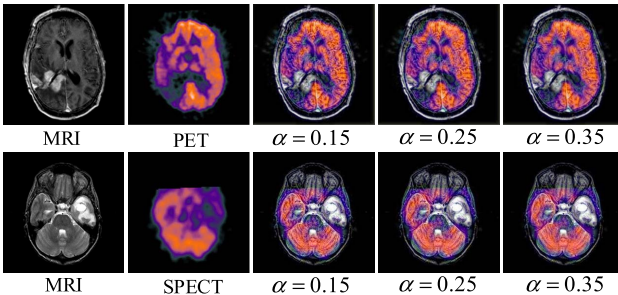
#### B. Experimental Results and Discussions

In discussing the experimental results, we first consider the parameters (intensity threshold, detail parameter, and edge parameter) and step length  $L$  in LLF. Then, multi-scale analyses based on the same image fusion rules are compared to evaluate the superiority of the proposed multi-scale decomposition scheme. The following experimental results show differences in the visual effects and objective results of the image fusion rules in the proposed framework versus other image fusion rules. Finally, the proposed framework is compared with state-of-the-art fusion methods. Each value in Tables IV-VI is the average of 30 pairs of test medical imaging data.

1) *Discussion of Parameters in LLF*: In the proposed method, we want to preserve the edge sharpness and enhance the detail information in the fused image, illustrated in Section II. Therefore, the edge parameter  $\beta$  is set as 1. In Fig. 1, it shows the filtered image by applying LLF ( $\sigma_r = 0.4, \alpha = 0.25, \beta = 1$ ) on the gray and RGB natural images, illustrated in Section II. Figs. 3-4 provide examples of fused medical images using different values of parameters in LLF. In Fig. 3, lines 3-5 display the fused results using different values of intensity threshold  $\sigma_r$  in LLF ( $\alpha = 0.25, \beta = 1$ ). In Fig. 4, lines 3-5 display the fused results using different values of detail parameter  $\alpha$  in LLF ( $\sigma_r = 0.4, \beta = 1$ ). It can be observed that the bigger the values of intensity threshold  $\sigma_r$  and detail parameter  $\alpha$  are, the more edge information fused results contain. However, noise exists in the fused medical images using the largest value of intensity threshold in LLF ( $\sigma_r = 0.6, \alpha = 0.25, \beta = 1$ ) and the largest value of detail parameter in LLF ( $\sigma_r = 0.4, \alpha = 0.35, \beta = 1$ ). Furthermore, Table II lists the objective results of the fused images with different parameters in LLF. The fused image using values ( $\sigma_r = 0.4, \alpha = 0.25, \beta = 1$ ) in LLF gets the best in terms of the metric *SSEQ*, marked in boldface in Table II. In conclusion, the intensity threshold  $\sigma_r$  is set as 0.4, the detail parameter  $\alpha$  is set as 0.25, and the edge parameter  $\beta$  is set as 1 in LLF.

TABLE II  
THE OBJECTIVE EVALUATION OF THE PARAMETERS IN LLF ( $\sigma_r$  DENOTES INTENSITY THRESHOLD,  
 $\alpha$  DENOTES DETAIL PARAMETER, AND  $\beta$  DENOTES EDGE PARAMETER)

	Metric	LLF+IOI ( $\sigma_r = 0.2$ )	LLF+IOI ( $\sigma_r = 0.4$ )	LLF+IOI ( $\sigma_r = 0.6$ )
$\alpha = 0.25, \beta = 1$	MRI-PET	SSEQ	50.7177	<b>49.8435</b>
	MRI-SPECT	SSEQ	53.9747	<b>53.7420</b>
$\sigma_r = 0.4, \beta = 1$	MRI-PET	SSEQ	50.2093	<b>49.8435</b>
	MRI-SPECT	SSEQ	53.9372	<b>53.7420</b>

Fig. 3. Discussion of intensity threshold  $\sigma_r$  in LLF.Fig. 4. Discussion of detail parameter  $\alpha$  in LLF.

2) *Discussion of Length L in LLF:* In this subsection, we study the impact of the length parameter  $L$  in LLF with the parameters ( $\sigma_r = 0.4$ ,  $\alpha = 0.25$ , and  $\beta = 1$ ) for MRI-PET and MRI-SPECT image fusion when the spatial resolution of all the test data is in  $256 \times 256$  pixels. Figs. 5-6 show the fused images with different lengths for LLF. LLF+IOI(2), LLF+IOI(3), LLF+IOI(4), and LLF+IOI(5) mean that the fusion method includes an image decomposition scheme: LLF with a step length of 2, 3, 4, and 5, respectively, and the IOI image fusion rules. From Fig. 5, it can be clearly observed that LLF+IOI(3) preserves the structure of soft-tissue from the input MRI image and preserves the blue background without color distortion from the input PET image. However, LLF+IOI(4) and LLF+IOI(5) methods introduce color distortion as seen in the red rectangular boxes in Fig. 5e-f. In Fig. 6, LLF+IOI(4) and LLF+IOI(5) introduce color distortion. LLF+IOI(2) method fails to preserve higher contrast of structural information, shown in Fig. 6c. However, the LLF+IOI(3) method retains both structural information and color information, shown in Fig. 6d. In addition to a subjective evaluation of the fused images by LLF with different lengths  $L$ , the objective metric values of  $EI$  are displayed in Table III [43], [44]. LLF+IOI(3) has the largest value in terms of the  $EI$  metric, that is, the best fused image occurs with a step length  $L = 3$ . In conclusion, step length  $L$

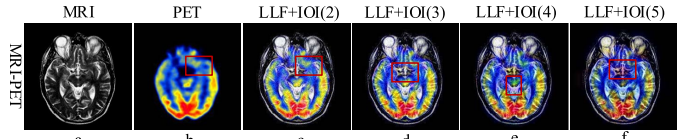


Fig. 5. Discussion of length  $L$  in LLF for MRI-PET image fusion. (a) MRI. (b) PET. (c) Image decomposition scheme LLF with the length of 2 and image fusion rule IOI. (d) Image decomposition scheme LLF with the length of 3 and image fusion rule IOI. (e) Image decomposition scheme LLF with the length of 4 and image fusion rule IOI. (f) Image decomposition scheme LLF with the length of 5 and image fusion rule IOI.

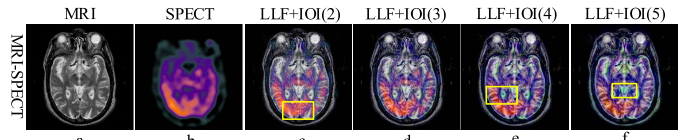


Fig. 6. Discussion of length  $L$  in LLF for MRI-SPECT image fusion. (a) MRI. (b) SPECT. (c) Image decomposition scheme LLF with the length of 2 and image fusion rule IOI. (d) Image decomposition scheme LLF with the length of 3 and image fusion rule IOI. (e) Image decomposition scheme LLF with the length of 4 and image fusion rule IOI. (f) Image decomposition scheme LLF with the length of 5 and image fusion rule IOI.

TABLE III  
THE OBJECTIVE EVALUATION OF STEP LENGTH  $L$   
WITH VALUES 2-5 IN LLF

Metric	LLF+IOI(2)	LLF+IOI(3)	LLF+IOI(4)	LLF+IOI(5)
MRI-PET	0.3688	<b>0.3821</b>	0.3709	0.3737
MRI-SPECT	0.3394	<b>0.3626</b>	0.3623	0.3602

is set to 3 because of better performance in terms of both subjective evaluation and objective evaluation. For all the test data with a spatial resolution of  $256 \times 256$  in the paper (see below), the default value of  $L$  in LLF is 3.

3) *Experimental Results on the Image Decomposition Schemes:* As shown in Figs. 7-8, 60 pairs of source images are grouped into two categories: MRI-PET and MRI-SPECT fusion to verify the effectiveness of the new image decomposition scheme: LLF with the parameters ( $\sigma_r = 0.4$ ,  $\alpha = 0.25$ , and  $\beta = 1$ ) for the proposed method. The proposed image decomposition scheme, LLF, is compared to LAP [10], COT [13], CVT [12], NSCT [17], and ST [14] using the same image fusion rule: Average-maximum. The average-maximum image fusion rule means that the fused low frequency images are defined as the average of low frequency images and the fused high frequency images are used to choose the maximum. Three pairs of MRI-PET image fusion results are explained in Fig. 7. The fused images using LLF proposed in this paper not only preserve structural information, but also obtain higher intensity information. However, the CVT and ST methods

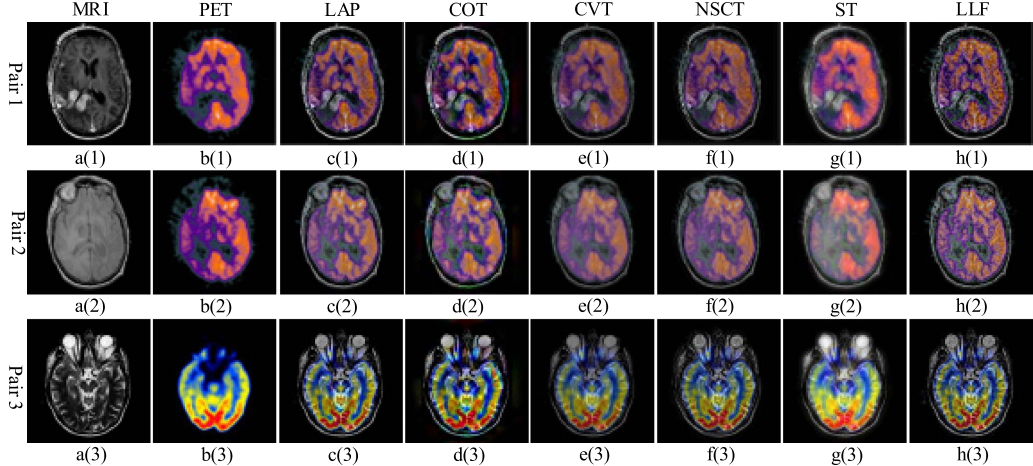


Fig. 7. The input MRI and PET images and the fused images using different multi-scale decomposition schemes. a(1)–a(3) Source image 1 MRI. b(1)–b(3) Source image 2 PET. c(1)–c(3) LAP. d(1)–d(3) COT. e(1)–e(3) CVT. f(1)–f(3) NSCT. G(1)–G(3) ST. h(1)–h(3) LLF.

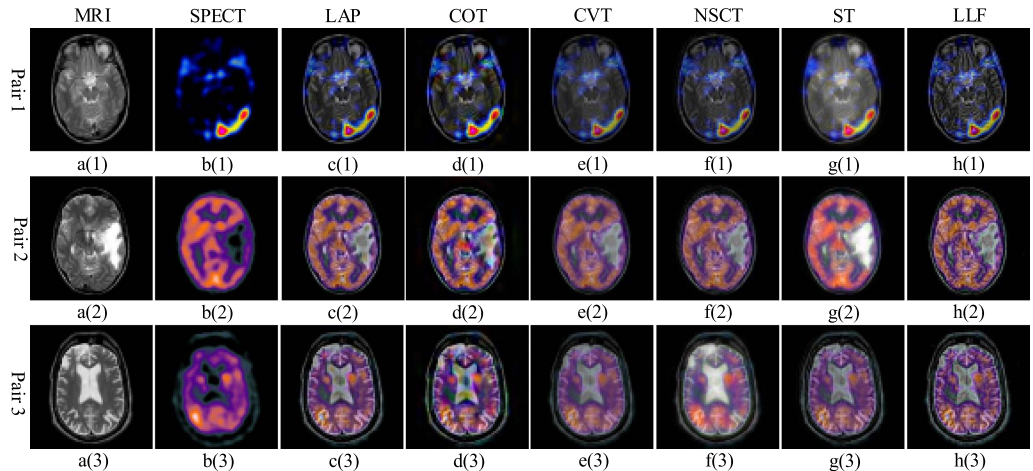


Fig. 8. The input MRI and SPECT images and the fused images using different multi-scale decomposition schemes. a(1)–a(3) Source image 1 MRI. b(1)–b(3) Source image 2 SPECT. c(1)–c(3) LAP. d(1)–d(3) COT. e(1)–e(3) CVT. f(1)–f(3) NSCT. G(1)–G(3) ST. h(1)–h(3) LLF.

are inferior with regards to detail information of structure while the ST method is superior with regards to luminance from the input functional PET image. For image pair 2 in Fig. 7, the fused results using the COT and NSCT methods generate color distortion and artifacts. Fig. 8 shows the fused images generated from the input MRI and SPECT images. By carefully observing image pair 1 in Fig. 8, the LLF method proposed in this study perfectly combines structural and intensity information. Furthermore, detail information in result image is enhanced by LLF. Unfortunately, color distortion problem exists in the result by COT method. As for image pair 2 in Fig. 8, white region represents brain tumor in MRI image. In Fig. 8g(2), the white regions in the input MRI image is absolutely preserved in the fused image using the ST method, but it is difficult to detect the brain tumor.

Table IV shows a quantitative assessment of the six fusion methods using the metrics *SSIM*, *STD*, *EI*, *SF*, and *AG* [24], [29], [42]–[46]. The value is the average of 30 sets of test images. The best value in Table IV is highlighted in boldface. It can be clearly observed that LLF proposed in this study performs best in terms of the *EI*, *SF*, and *AG* metrics for MRI-PET and MRI-SPECT fusion. This finding means that the fused image obtained by LLF contains much more gradient

information, such as edge and structural information. On the other hand, the LAP method performs best in terms of the metrics *SSIM* and *STD* (values in boldface in Table IV). *STD* and *SSIM* metrics measure the contrast information of the fused image quality using variance [52]–[54]. Since LAP [10] is the difference between the successive levels of the low-pass filtered image, to preserve the contrast information in the input images, LAP has larger values for the *SSIM* and *STD* metrics than LLF. However, LAP is unable to represent edge information well, because LAP needs the spatially invariant Gaussian kernels in the low-pass filter. *EI* is a no-reference metric. The sharper the edges are, the sharper the image is. *AG* shows the sharpness of the fused image. *SF* indicates the overall activity level in the fused image based on the local intensity variation. Therefore, LLF performs better in terms of *EI*, *SF*, and *AG* metrics than LAP.

**4) Experimental Results on the Image Fusion Rules:** As shown in Figs. 9–10, 60 pairs of source images are grouped into two categories: MRI-PET fusion and MRI-SPECT fusion to verify the effectiveness of the new image fusion rule: IOI in the proposed method. Image fusion rule refers to combining the decomposed images into a single image. We compare IOI with five fusion methods including PCA [20], GIHS [21],

TABLE IV  
THE OBJECTIVE EVALUATION OF DIFFERENT MULTI-SCALE DECOMPOSITION SCHEMES

	Metrics	LAP	COT	CVT	NSCT	ST	LLF
MRI-PET	<i>SSIM</i>	<b>0.6254</b>	0.5982	0.3559	0.4394	0.4255	0.5737
	<i>STD</i>	<b>1.4333</b>	1.3357	1.4135	1.3309	1.2182	1.4234
	<i>EI</i>	61.9004	40.8361	61.7983	55.7492	42.5176	<b>80.6514</b>
	<i>SF</i>	21.0988	15.0515	20.3245	17.6139	12.6316	<b>27.0119</b>
MRI-SPECT	<i>AG</i>	6.1117	4.1657	6.0487	5.5267	4.1085	<b>8.4013</b>
	<i>SSIM</i>	<b>0.6267</b>	0.6041	0.3705	0.4501	0.4840	0.5835
	<i>STD</i>	<b>1.4149</b>	1.3218	1.4137	1.3233	1.2528	1.4130
	<i>EI</i>	53.6294	34.5445	54.5668	49.0709	35.4475	<b>74.3072</b>
MRI-SPECT	<i>SF</i>	18.1239	12.8109	17.8269	15.5657	10.8852	<b>24.7330</b>
	<i>AG</i>	5.2407	3.4808	5.2924	4.8486	3.4085	<b>7.6429</b>

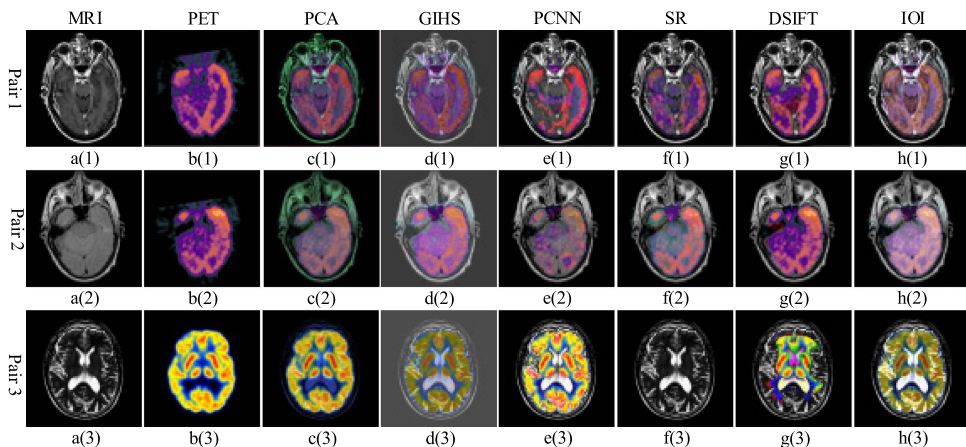


Fig. 9. The input MRI and PET images and the fused images using different image fusion rules. a(1)–a(3) Source image 1 MRI. b(1)–b(3) Source image 2 PET. c(1)–c(3) PCA. d(1)–d(3) GIHS. e(1)–e(3) PCNN f(1)–f(3) SR. G(1)–G(3) DSIFT. h(1)–h(3) IOI.

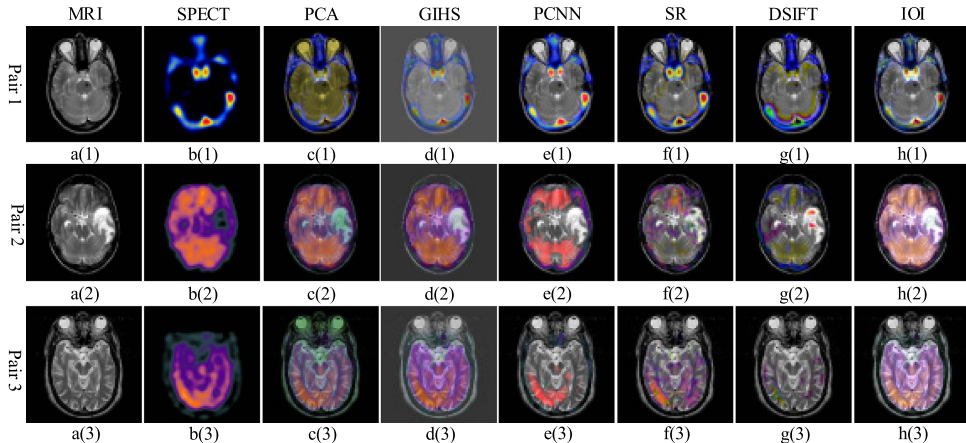


Fig. 10. The input MRI and SPECT images and the fused images using different image fusion rules. a(1)–a(3) Source image 1 MRI. b(1)–b(3) Source image 2 SPECT. c(1)–c(3) PCA. d(1)–d(3) GIHS. e(1)–e(3) PCNN f(1)–f(3) SR. G(1)–G(3) DSIFT. h(1)–h(3) IOI.

PCNN [22], SR [24], and DSIFT [8]. Fig. 9 explains the results of MRI-PET fusion. The images obtained using the IOI based rule show high contrast but low luminance. Color distortion is observed when combining the input images generated by the PCA method. The GIHS method inserts gray in the background in Fig. 9d(1)-d(3). For image pair 3 shown in Fig. 9, the fused image using the SR method looks similar to the input MRI image while losing the functional information from the PET image. Moreover, DSIFT method preserves part of the color information. Fig. 10 illustrates the performance of the fusion methods on MRI-SPECT fusion. Although the GIHS

method preserves both structural and functional information, the results using the GIHS method are presented in grayscale. PCNN, SR, and DSIFT methods retain a small amount of color information from the SPECT image. In Table V, the averaged values of 30 data sets are given. The proposed IOI based fusion rule performs best in terms of the metrics *MI* and *TMQI*. Both the *MI* and *TMQI* metrics are computed using the reference image. That is, much more structural and statistical information from the input anatomical image (MRI) and the functional image (PET and SPECT) has been transferred to the fused image.

TABLE V  
THE OBJECTIVE EVALUATION OF DIFFERENT IMAGE FUSION RULES

	Metrics	PCA	GIHS	PCNN	SR	DSIFT	IOI
MRI-PET	<i>MI</i>	5.0997	4.9520	5.2151	4.9958	5.0885	<b>5.2348</b>
	<i>GMS</i>	0.1878	0.1982	0.2246	0.2008	<b>0.2275</b>	0.2040
	<i>VIF</i>	0.2891	0.3998	0.2837	<b>0.4074</b>	0.3677	0.3492
	<i>TMQI</i>	0.7239	0.6986	0.7276	0.6990	0.7047	<b>0.7468</b>
MRI-SPECT	<i>SSEQ</i>	53.1465	<b>52.9409</b>	53.6295	53.1630	53.6161	53.9674
	<i>MI</i>	5.0254	4.9146	5.2550	4.6000	5.0314	<b>5.2754</b>
	<i>GMS</i>	0.1654	<b>0.2009</b>	0.2000	0.1922	0.1916	0.1834
	<i>VIF</i>	0.3196	0.3157	0.3070	0.2912	0.3599	<b>0.3605</b>
MRI-SPECT	<i>TMQI</i>	0.7203	0.7156	0.7263	0.7298	0.7048	<b>0.7479</b>
	<i>SSEQ</i>	<b>53.6587</b>	53.9890	54.0828	54.0299	53.9549	53.9688

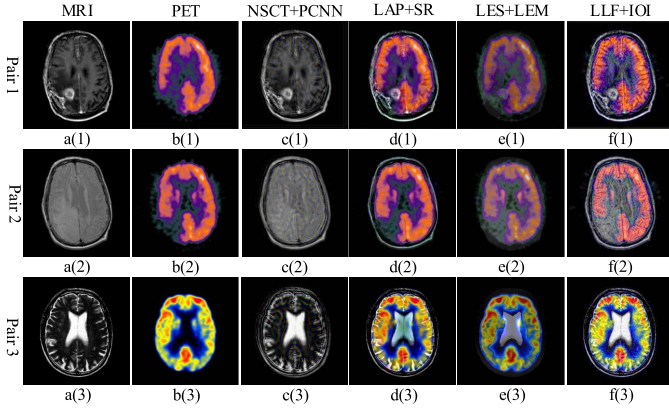


Fig. 11. The input MRI and PET images and the fused images using different fusion methods. a(1)–a(3) Source image 1 MRI. b(1)–b(3) Source image 2 PET. c(1)–c(3) NSCT+PCNN. d(1)–d(3) LAP+SR. e(1)–e(3) LES+LEM. f(1)–f(3) LLF+IOI.

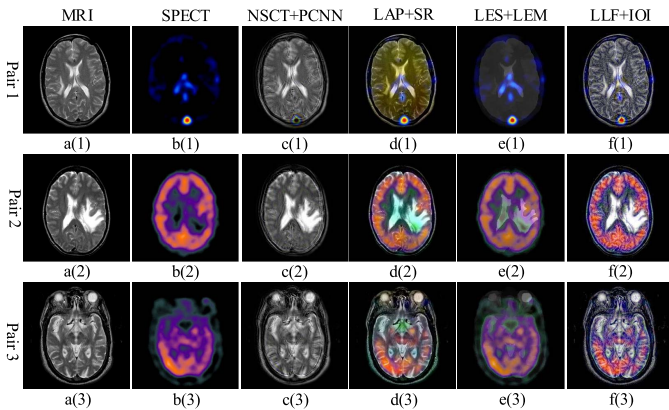


Fig. 12. The input MRI and SPECT images and the fused images using different fusion methods. a(1)–a(3) Source image 1 MRI. b(1)–b(3) Source image 2 SPECT. c(1)–c(3) NSCT+PCNN. d(1)–d(3) LAP+SR. e(1)–e(3) LES+LEM. f(1)–f(3) LLF+IOI.

5) *Overall Comparison:* To demonstrate the effectiveness of the proposed method: LLF+IOI with the parameters ( $\sigma_r = 0.4$ ,  $\alpha = 0.25$ , and  $\beta = 1$ ), the experiments are compared to three state-of-the-art methods: NSCT+PCNN [23], LAP+SR [24], and LES+LEM [55]. The test image data contain 30 sets of MRI and PET images and 30 sets of MRI and SPECT images. The fused images using the different methods are shown in Figs. 11–12. For MRI-PET image fusion,

TABLE VI  
THE OBJECTIVE EVALUATION OF DIFFERENT FUSION METHODS

	Metrics	NSCT+PCNN	LAP+SR	LES+LEM	LLF+IOI
MRI-PET	<i>SF</i>	8.3372	20.6514	18.9951	<b>25.2977</b>
	<i>EI</i>	23.3569	61.3878	61.4546	<b>78.7617</b>
	<i>MI</i>	4.8251	<b>4.9415</b>	4.3649	4.8876
	<i>TMQI</i>	0.7153	0.7282	0.6802	<b>0.7328</b>
MRI-SPECT	<i>SF</i>	6.9528	18.1440	16.4772	<b>23.3339</b>
	<i>EI</i>	18.4146	54.7703	54.3136	<b>74.5088</b>
	<i>MI</i>	4.7633	4.8185	4.2760	<b>4.9059</b>
	<i>TMQI</i>	0.7241	<b>0.7294</b>	0.6920	0.7292

it can be seen from Fig. 11 that the proposed LLF+IOI method preserves considerable intensity information and enhances detail information. However, there is almost no color information in the results using the NSCT+PCNN method. The LAP+SR and LES+LEM methods generate color distortion, as seen in Fig. 11d(3) and e(3). For MRI-SPECT image fusion, the proposed method not only enhances the detail information, but also preserves the regions of high intensity. Table VI provides an objective assessment in terms of the *SF*, *EI*, *MI*, and *TMQI* metrics [29], [43], [44], [47], [50]. For MRI-PET fusion, the proposed LLF+IOI method generates the largest value for the *SF*, *EI*, and *TMQI* metrics. Moreover, the LLF+IOI method performs best based on the *SF*, *EI*, and *MI* metrics for MRI-SPECT fusion.

From Figs. 7–12 and Tables. IV–VI, the following can be concluded:

(1) The image decomposition scheme LLF contributes to enhanced structural information originating from the input MRI image.

(2) The IOI-based image fusion rule is good at preserving luminance from the input PET and SPECT image.

(3) Compared to the proposed method, the images generated using the NSCT+PCNN method are closely related to the decomposition scheme NSCT. In addition, the images generated using the LAP+SR method are related to the image fusion rule SR.

## V. CONCLUSIONS

In this paper, we propose a new multi-modal medical image fusion method that uses LLF (**Algorithm 1**). In the proposed method, based on the number of levels ( $L = 3$ ), the LLF descriptor is first used to decompose the input anatomical medical images and functional medical images into their

multi-scale image representations. Then, the LEM scheme (**Algorithm 2**) is generalized to enable fusing the approximate images. For the decomposed residual images, an IOI-based scheme provides the fusion rule. Finally, the output image is obtained using the inverse LLF. The proposed method is also compared with state-of-the-art fusion methods using ten objective metrics. The proposed method is available in MATLAB (R2012a) at <http://www.escience.cn/people/xiaomi/index.html>.

However, the limitations of the proposed method are: (1) LLF does not run as fast as other multi-scale tools. (2) The superiority of the proposed method is verified by the better metric values in tables. The statistical significance of such difference is unknown. (3) The proposed image fusion rule: IOI introduce less color information. Hence, there are some works carried out in the future. The first is to construct approximate filter to make the fusion method run faster. The second is to develop more effective image fusion rules for MRI-PET and MRI-SPECT image fusion while introducing few color distortion. Finally, statistical significance tools including non-parametric Friedman test and the post-hoc Bonferroni-Dunn test to evaluate the true difference between different fusion methods using objective metric values.

## REFERENCES

- [1] A. P. James and B. V. Dasarathy, "Medical image fusion: A survey of the state of the art," *Inf. Fusion*, vol. 19, no. 3, pp. 4–19, 2013.
- [2] V. Barra and J.-Y. Boire, "A general framework for the fusion of anatomical and functional medical images," *NeuroImage*, vol. 13, no. 3, pp. 410–424, 2001.
- [3] P. Ganasala and V. Kumar, "Multimodality medical image fusion based on new features in NSST domain," *Biomed. Eng. Lett.*, vol. 4, no. 4, pp. 414–424, 2014.
- [4] B. Weissler *et al.*, "A digital preclinical PET/MRI insert and initial results," *IEEE Trans. Med. Imag.*, vol. 34, no. 11, pp. 2258–2270, Nov. 2015.
- [5] H. F. Wehrl, A. W. Sauter, M. R. Divine, and B. J. Pichler, "Combined PET/MR: A technology becomes mature," *J. Nucl. Med.*, vol. 56, no. 2, pp. 165–168, 2015.
- [6] C. Grova *et al.*, "A methodology for generating normal and pathological brain perfusion SPECT images for evaluation of MRI/SPECT fusion methods: Application in epilepsy," *Phys. Med. Biol.*, vol. 48, no. 24, pp. 4023–4043, 2003.
- [7] L. Klein, *Sensor and Data Fusion Concepts and Applications*. Bellingham, WA, USA: SPIE, 1999.
- [8] Y. Liu, S. Liu, and Z. Wang, "Multi-focus image fusion with dense SIFT," *Inf. Fusion*, vol. 23, pp. 139–155, May 2015.
- [9] G. Piella, "A general framework for multiresolution image fusion: From pixels to regions," *Inf. Fusion*, vol. 4, no. 4, pp. 259–280, 2003.
- [10] P. J. Burt and E. H. Adelson, "The Laplacian pyramid as a compact image code," *IEEE Trans. Commun.*, vol. COM-31, no. 4, pp. 532–540, Apr. 1983.
- [11] A. Toet, "Hierarchical image fusion," *Mach. Vis. Appl.*, vol. 3, no. 1, pp. 1–11, 1990.
- [12] E. Candès, L. Demanet, D. Donoho, and X. Ying, "Fast discrete curvelet transforms," *Multiscale Model. Simul.*, vol. 5, no. 3, pp. 861–899, Sep. 2006.
- [13] S. Yang *et al.*, "Image fusion based on a new contourlet packet," *Inf. Fusion*, vol. 11, no. 2, pp. 78–84, 2010.
- [14] Q.-G. Miao, C. Shi, P.-F. Xu, M. Yang, and Y.-B. Shi, "A novel algorithm of image fusion using shearlets," *Opt. Commun.*, vol. 284, no. 6, pp. 1540–1547, 2011.
- [15] A. L. da Cunha, J. Zhou, and M. N. Do, "The nonsubsampled contourlet transform: Theory, design, and applications," *IEEE Trans. Image Process.*, vol. 15, no. 10, pp. 3089–3101, Oct. 2006.
- [16] G. Easley, D. Labate, and W.-Q. Lim, "Sparse directional image representations using the discrete shearlet transform," *Appl. Comput. Harmon. Anal.*, vol. 25, no. 1, pp. 25–46, Jul. 2008.
- [17] G. Bhatnagar, Q. M. J. Wu, and Z. Liu, "Directive contrast based multimodal medical image fusion in NSCT domain," *IEEE Trans. Multimedia*, vol. 15, no. 5, pp. 1014–1024, Aug. 2013.
- [18] Z. Sheng, Z. S. Wen, J. Liu, G.-X. Zhu, and J.-W. Tian, "Multisource image fusion method using support value transform," *IEEE Trans. Image Process.*, vol. 16, no. 7, pp. 1831–1839, Jul. 2007.
- [19] H. Zhao, Z. Shang, Y. Y. Tang, and B. Fang, "Multi-focus image fusion based on the neighbor distance," *Pattern Recognit.*, vol. 46, pp. 1002–1011, Mar. 2013.
- [20] H. R. Shahdoosti and H. Ghassanian, "Combining the spectral PCA and spatial PCA fusion methods by an optimal filter," *Inf. Fusion*, no. 27, pp. 150–160, 2016.
- [21] M. Choi, "A new intensity-hue-saturation fusion approach to image fusion with a tradeoff parameter," *IEEE Trans. Geosci. Remote Sens.*, vol. 44, no. 6, pp. 1672–1682, Jun. 2006.
- [22] M. M. Subashini and S. K. Sahoo, "Pulse coupled neural networks and its applications," *Expert Syst. Appl.*, vol. 41, no. 8, pp. 3965–3974, 2014.
- [23] Q. Xiao-Bo, Y. Jing-Wen, X. I. A. O. Hong-Zhi, and Z. Zi-Qian, "Image fusion algorithm based on spatial frequency-motivated pulse coupled neural networks in nonsubsampled contourlet transform domain," *Acta Autom. Sinica*, vol. 34, no. 12, pp. 1508–1514, 2008.
- [24] Y. Liu, S. Liu, and Z. Wang, "A general framework for image fusion based on multi-scale transform and sparse representation," *Inf. Fusion*, vol. 24, pp. 147–164, Jul. 2015.
- [25] G. Bhatnagar, Q. M. J. Wu, and Z. Liu, "Human visual system inspired multi-modal medical image fusion framework," *Expert Syst. Appl.*, vol. 40, no. 5, pp. 1708–1720, 2013.
- [26] S. S. Paris, S. W. Hasinoff, and J. Kautz, "Local Laplacian filters: Edge-aware image processing with a Laplacian pyramid," *ACM Trans. Graph.*, vol. 30, no. 4, pp. 1244–1259, 2011.
- [27] J. Wang, H. Zha, and R. Cipolla, "Combining interest points and edges for content-based image retrieval," in *Proc. IEEE Int. Conf. Image Process.*, Sep. 2005, pp. 1256–1259.
- [28] K. Subr, C. Soler, and F. Durand, "Edge-preserving multiscale image decomposition based on local extrema," *ACM Trans. Graph.*, vol. 28, no. 5, p. 147, 2009.
- [29] Y. Zheng *et al.*, "A new metric based on extended spatial frequency and its application to DWT based fusion algorithms," *Inf. Fusion*, vol. 8, no. 2, pp. 177–192, 2007.
- [30] H. Soltanian-Zadeh, J. P. Windham, and A. E. Yagle, "A multidimensional nonlinear edge-preserving filter for magnetic resonance image restoration," *IEEE Trans. Image Process.*, vol. 4, no. 2, pp. 147–161, Feb. 1995.
- [31] J. Langner *et al.*, "Locally adaptive filtering for edge preserving noise reduction on images with low SNR in PET," in *Proc. Nucl. Sci. Symp. Med. Imag. Conf.*, 2011, pp. 3102–3104.
- [32] S. Li, X. Kang, and J. Hu, "Image fusion with guided filtering," *IEEE Trans. Image Process.*, vol. 22, no. 7, pp. 2864–2875, Jul. 2013.
- [33] Y. Jiang and M. Wang, "Image fusion using multiscale edge-preserving decomposition based on weighted least squares filter," *IET Image Process.*, vol. 8, no. 3, pp. 183–190, Mar. 2014.
- [34] J. Hu and S. Li, "The multiscale directional bilateral filter and its application to multisensor image fusion," *Inf. Fusion*, vol. 13, no. 3, pp. 196–206, 2012.
- [35] W. Li, Z. Zhao, J. Du, and Y. Wang, "Edge-preserve filter image enhancement with application to medical image fusion," *J. Med. Imag. Health Inf.*, vol. 7, no. 1, pp. 16–24, 2017.
- [36] R. S. Blum, *Multi-Sensor Image Fusion and its Applications*. Boca Raton, FL, USA: CRC Press, 2005.
- [37] R. Shen, I. Cheng, and A. Basu, "Cross-scale coefficient selection for volumetric medical image fusion," *IEEE Trans. Biomed. Eng.*, vol. 60, no. 4, pp. 1069–1079, Apr. 2013.
- [38] K. A. Johnson and J. A. Becker, *The Whole Brain ALTAS*. Accessed: 1999. [Online]. Available: <http://www.med.harvard.edu/aanlib/>
- [39] L. Wang, B. Li, and L.-F. Tian, "EGGDD: An explicit dependency model for multi-modal medical image fusion in shift-invariant shearlet transform domain," *Inf. Fusion*, vol. 19, no. 11, pp. 29–37, Sep. 2014.
- [40] S. Daneshvar and H. Ghassanian, "MRI and PET image fusion by combining IHS and retina-inspired models," *Inf. Fusion*, vol. 11, no. 2, pp. 114–123, 2010.
- [41] Z. Wang and Y. Ma, "Medical image fusion using *m*-PCNN," *Inf. Fusion*, vol. 9, no. 2, pp. 176–185, 2008.
- [42] Z. Wang, A. C. Bovik, H. R. Sheikh, and E. P. Simoncelli, "Image quality assessment: From error visibility to structural similarity," *IEEE Trans. Image Process.*, vol. 13, no. 4, pp. 600–612, Apr. 2004.

- [43] Y. Wang *et al.*, "A no-reference perceptual blur metric based on complex edge analysis," in *Proc. IEEE Int. Conf. Netw. Infrastruct. Digit. Content*, Sep. 2013, pp. 487–491.
- [44] X. Ma *et al.*, "A no-reference image blur metric based on two-pass edge analysis," in *Proc. Int. Conf. Natural Comput.*, 2015, pp. 919–924.
- [45] R. Singh and A. Khare, "Multiscale medical image fusion in wavelet domain," *Sci. World J.*, vol. 5, Dec. 2013, Art. no. 521034.
- [46] N. Chabi, M. Yazdi, and M. Entezarmahdi, "An efficient image fusion method based on dual tree complex wavelet transform," in *Proc. 8th Iranian Conf. Mach. Vis. Image Process.*, 2013, pp. 403–407.
- [47] M. Hossny, S. Nahavandi, and D. Creighton, "Comments on 'Information measure for performance of image fusion,'" *Electron. Lett.*, vol. 44, no. 18, pp. 1066–1067, 2008.
- [48] W. Xue, L. Zhang, X. Mou, and A. C. Bovik, "Gradient magnitude similarity deviation: A highly efficient perceptual image quality index," *IEEE Trans. Image Process.*, vol. 23, no. 2, pp. 684–695, Feb. 2014.
- [49] H. R. Sheikh and A. C. Bovik, "Image information and visual quality," *IEEE Trans. Image Process.*, vol. 15, no. 2, pp. 430–444, Feb. 2006.
- [50] H. Yeganeh and Z. Wang, "Objective quality assessment of tone-mapped images," *IEEE Trans. Image Process.*, vol. 22, no. 2, pp. 657–667, Feb. 2013.
- [51] L. Liu, B. Liu, H. Huang, and A. C. Bovik, "No-reference image quality assessment based on spatial and spectral entropies," *Signal Process., Image Commun.*, vol. 29, no. 8, pp. 856–863, 2014.
- [52] B. Kumar, S. B. Kumar, and C. Kumar, "Development of improved SSIM quality index for compressed medical images," in *Proc. IEEE 2nd Int. Conf. Image Inf. Process. (ICIIP)*, Dec. 2013, pp. 251–255.
- [53] S. S. Channappayya, A. C. Bovik, and R. W. Heath, Jr., "Rate bounds on SSIM index of quantized images," *IEEE Trans. Image Process.*, vol. 17, no. 9, pp. 1624–1639, Sep. 2008.
- [54] S. Das and M. K. Kundu, "A neuro-fuzzy approach for medical image fusion," *IEEE Trans. Biomed. Eng.*, vol. 60, no. 12, pp. 3347–3353, Dec. 2013.
- [55] Z. Xu, "Medical image fusion using multi-level local extrema," *Inf. Fusion*, vol. 19, no. 11, pp. 38–48, 2013.



**Jiao Du** received the M.S. and Ph.D. degrees from the Chongqing University of Posts and Telecommunications in 2013 and 2017, respectively. She is currently a Lecturer with the Chongqing Engineering Laboratory for Detection, Control and Integrated System, Chongqing Technology and Business University. Her research interests include pattern recognition and image processing.



**Weisheng Li** received the M.S. and Ph.D. degrees from Xidian University in 2000 and 2004, respectively. He is currently a Professor with the Chongqing University of Posts and Telecommunications. His research focuses on intelligent information processing and pattern recognition.



**Bin Xiao** received the B.S. and M.S. degrees from Shaanxi Normal University in 2004 and 2007, respectively, and the Ph.D. degree from Xidian University. He is an Associate Professor with the Chongqing University of Posts and Telecommunications. His research interests include image processing, pattern recognition, and digital watermarking.